



Originally published as:

Singh, A. K., Baumann, G., Henniges, J., Görke, U. J., Kolditz, O. (2012): Numerical analysis of thermal effects during carbon dioxide injection with enhanced gas recovery: a theoretical case study for the Altmark gas field. - *Environmental Earth Sciences*, 67, 2, 497-509

DOI: [10.1007/s12665-012-1689-9](https://doi.org/10.1007/s12665-012-1689-9)

## Numerical analysis of thermal effects during carbon dioxide injection with enhanced gas recovery: A theoretical case study for the Altmark gas field

A.K. Singh · G. Baumann · J. Henniges ·  
U.-J. Görke · O. Kolditz

Received: date / Accepted: date

**Abstract** Predictions about reservoir temperature change during carbon dioxide injection requires consideration of all, often-subtle, thermal effects. In particular, Joule-Thomson cooling (JTC) and the viscous heat dissipation (VHD) effect are factors that cause flowing fluid temperature to differ from the static formation temperature. In this work, warm-back behavior (thermal recovery after injection completed), as well as JTC and VHD effects, at a multi-layered depleted gas reservoir are demonstrated numerically. OpenGeoSys (OGS) is able to solve coupled partial differential equations for pressure, temperature and mole-fraction of each component of the mixture with a combination of monolithic and staggered approaches. The Galerkin finite element approach is adapted for space discretization of governing equations, whereas for temporal discretization a generalized implicit single-step scheme is used. For numerical modeling of warm-back behavior, we chose a simplified test case of carbon dioxide injection. This test case is numerically solved by using OGS and FeFlow simulators independently. OGS differs from FeFlow in the capability of representing multi-componential effects on warm-back behavior. We verify both code results by showing the close comparison of shut-in temperature profiles along the injection well. As the JTC cooling rate is inversely proportional to the volumetric heat capacity of the solid matrix, the injection layers are cooled faster compared to non-injection layers. The shut-in temperature profiles are showing a significant change in reservoir temperature; hence it is important to account to thermal effects in injection monitoring.

**Keywords** Distributed temperature sensing · Joule-Thomson cooling · multi-layered depleted gas reservoir · OpenGeoSys · shut-in temperature profile · viscous heat dissipation · volumetric heat capacity · warm-back

---

A.K. Singh · U.-J. Görke · O. Kolditz  
Department of Environmental Informatics  
Helmholtz Centre for Environmental Research-UFZ, Leipzig 04318, Germany  
Tel.: +49-341-235-1089; Fax: +49-341-235-1939  
E-mail: ashok.singh@ufz.de

G. Baumann · J. Henniges  
German Research Centre for Geosciences-GFZ, Potsdam 14473, Germany

## 1 Introduction

Enhanced gas recovery (EGR) is an important technology for gas production from depleted reservoirs (Oldenburg et al. (2004); Kühn et al. (2011); Yang et al. (2011); Becker et al. (2012)). To this purpose carbon dioxide is injected into the reservoir enhancing the natural gas production. The subsurface system consists basically of two elements, (i) wellbore and (ii) reservoir. Models are developed and used for controlling the thermodynamic processes within the wellbore to guarantee optimal carbon dioxide injectivity and characterizing large-scale reservoir properties to assess the long-term effects of EGR (Singh et al. (2011); Böttcher et al. (2011); Singh et al. (2012); Esposito et al. (2010)). Typically, gas reservoirs consist of multiple layers of different types of rock. Layers of the reservoir usually have different properties, such as thicknesses, porosities and permeabilities that tend to cause differential depletion during reservoir exploitation. Thermal conductivity of injecting carbon dioxide differs to most materials filling the pore space with the exception of natural gas, which is quite similar to it. Experimental studies by Ehlig-Economides and Joseph (1987) showed that transient temperature response is very sensitive to individual layers' permeability, porosity, thermal conductivity and specific heat capacity values. Sedimentary deposition processes of the multi-layer reservoir is analyzed by many researches (Ahmed and Lee (1995); Sui et al. (2008); Cui and Zhao (2010); Tenzer et al. (2010)) to quantify formation properties.

Temperature data can provide additional information to characterize hydraulic formation properties (Henninges et al. (2011); Henninges and Baumann (2012)). Finding of Mathias et al. (2010) indicate that during the injection of gas there are thermodynamic mechanisms which can change the reservoir temperature as the injection pressure drops. Firstly, cooling occurs due to the JTC process. At the entry point to the reservoir the injected gas expands significantly which increases the intermolecular potential and, consequently, gas temperature decreases following the energy conservation law. Secondly, heating can occur due to VHD as a result of energy conversion by friction. Additionally, investigations about heat transfer between injection and formation fluid (also between injection and non-injection layers) helps to analyze the warm-back phenomena. By shutting the well for a period of time, we are able to record the transient temperature response due to conductive heat transport.

One of the earliest works on the thermal behavior of fluid flow through boreholes was presented by Ramey (1961). He has developed a model for the prediction of wellbore fluid temperature as a function of depth. Additionally, Ramey (1961) expanded this approach to give the rate of heat loss from the well to the formation, assuming steady state in the wellbore and unsteady conductive heat transfer to the reservoir. Only few authors have studied so far the thermodynamics of fluid flow through multi-layer porous media, especially in the context of JTC and VHD. Lefkovits et al. (1961) developed a detailed mathematical description and studied the relative rates of layers depletion. Found that, rate of depletion is depending on permeability of the reservoir layers, i.e. more permeable layer have higher depletion rate compared to less permeable layer. In his work, the average formation properties can be determined using buildup curves. Following Lefkovits work, several authors improved his mathematical model. Analytical approach to investigate flow rate in production and injection wells is described by Witterholt and Tixier (1972); Curtis and Witterholt (1973). Hurter et al. (2007) detected carbon dioxide by adopting temperature logging technique in the framework of carbon dioxide storage. Ehlig-Economides and Joseph (1987) extended the model to

an arbitrary number of layers and included interlayer cross flow as well as the effects of wellbore storage. This study showed that individual layer properties in multi-layer reservoirs cannot be determined from conventional drawdown or buildup tests. A more general analytical solution for multi-layer testing in commingled reservoirs was presented by [Kuchuk et al. \(1991\)](#). Their approach is applicable to a variety of reservoir systems in which individual layers may have different initial and outer-boundary conditions. A complete literature review of the analytical models developed between the 1960s and the 1980s can be found in [Ehlig-Economides and Joseph \(1987\)](#).

[Oldenburg \(2007\)](#), performed numerical simulation to investigate the magnitude of JTC effect that may arise during carbon dioxide injection into depleted methane reservoir with using EOS7C (is a module of TOUGH2). He mentioned that JTC effect could produce extreme cold in the subsurface which generates thermal stresses that could fracture the formation. Most commonly, these effects are considered as part of wellbore and completion modeling where pressure drops can be significant ([Ouyang and Belanger \(2006\)](#)). [Ramazanov and Nagimov \(2007\)](#) presented an analytical model to estimate the temperature distribution in a saturated porous formation with variable bottomhole pressure. They solved the convective heat transport model with variable pressure but constant flow rate. Their investigation showed that pressure drop can change reservoir temperature. [Pruess \(2008\)](#) did numerical simulation to study the temperature effect on carbon dioxide leakage from geologic storage. He pointed out that pressure decrease and associated heat exchange is isenthalpic, when carbon dioxide migrates upward. Monitoring carbon dioxide injection in the framework of enhanced gas recovery (EGR) operations is a current research target. [Mathias et al. \(2010\)](#) derived an analytical solution by invoking steady-state flow and constant thermo-physical properties. They compared results from isothermal and non-isothermal simulations using this analytical solution. [Andre et al. \(2010\)](#) investigated the JTC effect associated with vaporization and dissolution of carbon dioxide. They have mentioned that JTC induce temperature changes which are significantly with combination of other thermal processes.

Within this study we present a numerical model to simulate the injection of carbon dioxide in a multi-layer depleted gas reservoir, which is filled with a homogeneous mixture of methane and nitrogen gases. This work is focused on the prediction of temperature changes in order to evaluate if temperature monitoring can be used for injection monitoring ([Henninges et al. \(2011\)](#); [Henninges and Baumann \(2012\)](#)). Through temperature monitoring it is possible to observe the injection section of the wellbore and identify the excessive gas influx. This information can potentially be inverted to infer the types and amounts of fluid entering along the wellbore. We are also interested in showing how reservoir temperature varies near the wellbore with fluid flowing through it. To this end, we perform simulations by taking into account heat loss due to gas expansion, and frictional heating along with conduction and convection. Governing equations for flow and heat transport processes are mass and energy balance equations, respectively. Sequentially, we solve fractional mass transport equations for the solution of the mole-fraction of mixture components. The selected primary variables, i.e. mixture pressure, temperature and mole-fractions of each component, respectively. For process coupling, we adopt a staggered approach. We use the finite element method (FEM) for solving the non-linear coupled, non-isothermal compositional gas flow (THC<sup>3</sup>) problem. The numerical model is implemented into the open source, scientific modeling platform OGS (e.g. [Rink et al. \(2011\)](#), [Wang et al. \(2011a\)](#)), and, therefore, other test cases have been considered. Material parameters changes with pressure, temperature and compo-

sitions; details about relationships have been presented in [Singh et al. \(2011\)](#). Process verification against analytical solutions has already been presented in a previous paper (see [Singh et al. \(2011\)](#); [Böttcher et al. \(2011\)](#)). For verification purposes we compared numerical results by OGS and FeFlow for a simplified (constant material parameters and injection and formation fluid are carbon dioxide) test case for a warm-back scenario in a multi-layered gas reservoir. Other test examples for single-layer problems can be found in [Böttcher et al. \(2011\)](#); [Kolditz et al. \(2012\)](#). This research work has been performed within the context of the joint research project CLEAN representing a German research and development alliance of scientific and industrial partners ([Kühn et al. \(2011\)](#); [Kühn et al. \(2012\)](#)).

## 2 Mathematical model

During carbon dioxide storage, analysis of fluid spreading into the gas reservoir needs pressure, temperature and mole-fraction of components. Mass balance equation gives the pressure and by using velocity, heat and fractional mass transport equations gives temperature and mole-fraction of components, respectively. In case of fluid flow through porous medium, Darcy's law is a good approximation for velocity field according to [Wooding \(2006\)](#); [Görke et al. \(2011\)](#); [Gray and Miller \(2004\)](#). In the following subsections, we briefly present the governing equations used in the non-isothermal compositional gas flow module of OGS.

### 2.1 Flow model

According to extended Darcy's law, the advective fluid flux is defined as

$$\mathbf{J}_a = \rho n \mathbf{v} = -\rho \frac{k}{\mu} (\nabla p - \rho \mathbf{g}) \quad (1)$$

where diffusive flux

$$\mathbf{J}_d = 0; \quad \mathbf{v} = \sum_{k=0}^2 x_k \mathbf{v}_k \quad (2)$$

Mixture density is according to extended ideal gas law  $\rho = M p / (zRT)$  ( $\text{kgm}^{-3}$ ), where super compressibility factor  $z$  is a dimensionless value accounts real behaviors of gas. Here,  $R$  ( $\text{Jkmol}^{-1}\text{K}^{-1}$ ) is universal gas constant;  $M$  ( $\text{kgkmol}^{-1}$ ) is mixture molecular weight;  $x$  is mole-fraction;  $\mathbf{v}$  ( $\text{ms}^{-1}$ ) is velocity vector;  $\mu$  (Pas) is mixture dynamic viscosity and  $\mathbf{g}$  ( $\text{ms}^{-2}$ ) is the gravity vector.  $n$  and  $k$  ( $\text{m}^2$ ) are the porosity and intrinsic permeability, respectively.

Mixture mass balance equation is in the following form

$$\frac{\partial(n\rho)}{\partial t} + \nabla \cdot \mathbf{J}_a = \rho Q_p; \quad (3)$$

where,  $t$  (s) is time and  $Q_p$  is source/ sink term.

## 2.2 Heat transport model

Following the assumption of local thermal equilibrium between fluid and solid matrix of the reservoir, the energy balance equation for the porous medium (which pores are filled with a mixture) is given as

$$(\rho c_p)_{\text{eff}} \frac{\partial T}{\partial t} + \rho c_p n \mathbf{v} \cdot \nabla T - \nabla \cdot [\kappa_{\text{eff}} \nabla T] = T \beta_T n \frac{\partial p}{\partial t} + (T \beta_T - 1) n \mathbf{v} \cdot \nabla p + Q_T \quad (4)$$

Here,  $c_p$  ( $\text{Jkg}^{-1}\text{K}^{-1}$ ) is specific heat capacity at constant pressure;  $Q_T$  is heat source/sink term. For the thermal expansion coefficient of the gaseous mixture  $\beta_T$  ( $\text{K}^{-1}$ ), we choose 0.003 to keep  $\mu_{\text{JT}} > 0$  (see Eq. (16)). Terms  $T \beta_T n \frac{\partial p}{\partial t}$  and  $T \beta_T n \mathbf{v} \cdot \nabla p$  are accounting JTC whereas term  $n \mathbf{v} \cdot \nabla p$  gives VHD effect. Condition under which the JTC and/or VHD processes should be taken into account was examined by [Garg and Pritchett \(1977\)](#). They suggest that if one wishes to account the pressure-work, then keep the viscous dissipation term in the energy balance Eq. (4).

Effective thermal conductivity coefficient is defined by  $\kappa_{\text{eff}} = (1 - n)\kappa^s + n\kappa$ . Effective volumetric heat capacity is defined by  $(\rho c_p)_{\text{eff}} = (1 - n)\rho^s c_p^s + n\rho c_p$ . 's' and 'eff' stand for solid phase and effective, respectively, further,  $\mu$ ,  $M$ ,  $c_p$  and  $\kappa$   $\text{Wm}^{-2}\text{K}^{-1}$  of the gaseous mixture are estimated by averaging over its components, while component's dynamic viscosity, specific heat capacity and thermal conductivity are density and temperature dependent. Medium properties of the solid matrix such as density, specific heat capacity and thermal conductivity were held constant.

## 2.3 Fractional mass transport model

The divergence form of the fractional mass transport equation is given by

$$n\rho \frac{\partial x_k}{\partial t} + \rho n \mathbf{v} \cdot \nabla x_k + x_k \rho Q_{\rho_p} - \nabla \cdot [n\rho \mathbf{D} \nabla x_k] = Q_{x_k}. \quad (5)$$

where  $\mathbf{D}$  is hydrodynamic dispersion tensor.

The dispersion process is controlled by  $\mathbf{D}$  ( $\text{m}^2\text{s}^{-1}$ ) which is assumed as homogeneous and isotropic. In porous media, diffusion cannot as fast as it can in free fluids because the fluid particles must follow longer pathways as they travel through pores of a solid skeleton. The product of diffusion coefficient  $D_k$  and the tortuosity factor  $\tau$ , i.e.  $\tau \mathbf{D}_k$  is often termed the effective diffusion coefficient. The tortuosity factor is estimated according to the empirical correlation  $\tau = \sqrt[3]{n}$  proposed by [Millington \(1961\)](#).

We have combined the tensors (diffusion and dispersion) in the tensor  $\mathbf{D}$ , defined by its tensor components

$$\mathbf{D} = D_{ij} = \tau D_k \delta_{ij} + \alpha_L |\mathbf{v}| \delta_{ij} + \frac{v_i v_j}{|\mathbf{v}|} (\alpha_L - \alpha_T) \quad (6)$$

where  $\delta_{ij}$  is the Kronecker-delta (coordinates of the unit tensor). The transverse dispersivity  $\alpha_T = 1$  m and longitudinal dispersivity  $\alpha_L = 0.1$  m were used in this study.

The diffusion coefficients can be calculated by using binary diffusion coefficient under the condition of zero overall diffusive flux ([Helmig \(1997\)](#)).

$$D_k = \frac{1 - x_k}{\sum_i \frac{x_i}{D_{i,k}}}; \text{ for } i \neq k \quad (7)$$

The pressure and temperature dependent binary diffusion coefficient is calculated from

$$D_{i,k} = D_0 \frac{p_0}{p} \left( \frac{T}{T_0} \right)^\pi \quad (8)$$

For any arbitrary pair of gas component coefficient  $D_0$  and exponent  $\pi$  can be found in [Vargaftik \(1975\)](#).

### 3 Numerical approach

The method of weighted residual is applied to derive the weak forms of the governing partial differential Eqs. (3), (4) and (5)

$$\mathbf{C}_{pp} \dot{\bar{\mathbf{p}}} + \mathbf{C}_{pT} \dot{\bar{\mathbf{T}}} + (\mathbf{A}_{pp} + \mathbf{K}_{pp}) \bar{\mathbf{p}} + (\mathbf{A}_{pT} + \mathbf{K}_{pT}) \bar{\mathbf{T}} = \mathbf{f}_p \quad (9)$$

$$\mathbf{C}_{Tp} \dot{\bar{\mathbf{p}}} + \mathbf{C}_{TT} \dot{\bar{\mathbf{T}}} + (\mathbf{A}_{Tp} + \mathbf{K}_{Tp}) \bar{\mathbf{p}} + (\mathbf{A}_{TT} + \mathbf{K}_{TT}) \bar{\mathbf{T}} = \mathbf{f}_T \quad (10)$$

$$\mathbf{C}_{x_k} \dot{\bar{\mathbf{x}}}_k + (\mathbf{A}_{x_k} + \mathbf{K}_{x_k}) \bar{\mathbf{x}}_k = \mathbf{f}_{x_k}; k = 0, 1, 2 \quad (11)$$

Here,  $\bar{\mathbf{p}}(t)$ ,  $\bar{\mathbf{T}}(t)$  and  $\bar{\mathbf{x}}_k(t)$  are nodal value vector for pressure, temperature and mole-fraction unknowns, respectively.  $\mathbf{f}_p$ ,  $\mathbf{f}_T$  and  $\mathbf{f}_{x_k}$  are the right hand side vectors.  $\mathbf{C}$ ,  $\mathbf{A}$  and  $\mathbf{K}$  denote mass, advection and Laplace matrices, respectively. Elements of these matrices and right hand side vectors are given in the Appendix.

Space discretization of the governing equations is carried out by means of the Galerkin finite element approach. Pressure  $p(\mathbf{x}, t)$ , temperature  $T(\mathbf{x}, t)$  and mole-fraction  $x_k(\mathbf{x}, t)$  of each component are expressed over whole domain by the nodal value vector and global shape function matrices  $\mathbf{N}(\mathbf{x})$

$$p = \mathbf{N} \bar{\mathbf{p}}; \quad T = \mathbf{N} \bar{\mathbf{T}}; \quad x_k = \mathbf{N} \bar{\mathbf{x}}_k; \quad k = 0, 1, 2 \quad (12)$$

The system of coupled equations for pressure, temperature and mole-fraction is solved by using a combination of monolithic and staggered approaches. That is, within a time step, pressure and temperature are solved monolithically then the fractional mass transport equation is solved for each component with using velocity and temperature. This so-called staggered approach is executed until specific convergence criteria are satisfied ([Kolditz and Diersch \(1993\)](#); [Park et al. \(2011\)](#)). Since we apply the staggered scheme for coupling, all mole-fraction related terms of the coupled equations are shifted to the corresponding right hand side vector and all pressure and temperature related terms of the uncoupled equation to the corresponding right hand sides. Here, coupled terms are calculated at each Gauss point by interpolating node values.

#### 3.1 Temporal discretization

To approximate the solution of ordinary differential equations Eqs. (9)-(11), temporal discretization is performed by using a generalized implicit single-step scheme and considering relaxation term as follows

$$\dot{\bar{\phi}} = \frac{\bar{\phi}^{m+1} - \bar{\phi}^m}{\Delta t}; \quad \bar{\phi} = \theta \bar{\phi}^{m+1} + (1 - \theta) \bar{\phi}^m \quad (13)$$

Substituting Eq. (13) into Eqs. (9)-(11) results in the following discretized time stepping algebraic equations in matrix form

$$(\mathbf{M}_\phi + \theta \Delta t (\mathbf{A}_\phi + \mathbf{K}_\phi)) \bar{\phi}^{m+1} = [\mathbf{M}_\phi - (1 - \theta) \Delta t (\mathbf{A}_\phi + \mathbf{K}_\phi)] \bar{\phi}^m \quad (14)$$

where  $\bar{\phi} = \bar{\mathbf{p}}, \bar{\mathbf{T}}$  or  $\bar{\mathbf{x}}_k$ ;  $m$  and  $m + 1$  represent the previous and current time steps, respectively.  $\Delta t$  denotes time step size  $t^{m+1} - t^m$ ,  $\theta$  is an relaxation constant. For forward differences,  $\theta = 0$ ; for backward differences,  $\theta = 1$ . To guarantee numerical stability, we take  $\theta \geq 0.5$ , as at this value of relaxation factor, an unconditional stable algorithm is obtained. For instance,  $\theta = 0.5$  gives second order central implicit scheme. Then the Picard method is adopted to linearize the discretized equation.

#### 4 Numerical example

Appropriate injection state of carbon dioxide is the key questions for carbon dioxide injection into the Altensalzwedel depleted gas reservoir which is owned and operated by GDF SUEZ E&P Deutschland GmbH (GDF SUEZ). Various injection temperatures of carbon dioxide are considered for different purpose, i.e. (1) evaluation of thermodynamic phenomena during injection (JTC and VHD processes), (2) determination of reservoir properties by warm-back analysis and tracer tests (Singh et al. (2012)) as well as (3) carbon dioxide injection technology for large volumes. In case (2) of warm-back analysis the temperature of injecting carbon dioxide is 102 °C. This value of temperature is obtained by analytical calculation of heat transfer between formation and injecting carbon dioxide on the way from wellhead to top of the reservoir (at given reservoir conditions and parameters). However, for case (1) of JTC and VHD analysis, we assumed that injecting carbon dioxide and formation are at the same temperature (125 °C) before injection starts. This assumption neglects other kind of heat transfer and emphasizes only JTC and VHD effects. Altensalzwedel gas reservoir contains fifteen different layers, eight of which are injection layers. Hydraulic and thermal parameters of these layers are taken from available well log data provided by GDF SUEZ (2009). Injection layers share a common density  $\rho^s = 2650 \text{ kgm}^{-3}$ , specific heat capacity  $c_p^s = 960 \text{ Jkg}^{-1}\text{K}^{-1}$  and thermal conductivity  $\kappa^s = 2.77 \text{ Wm}^{-1}\text{K}^{-1}$ , but porosity and intrinsic permeability are different (averaged value, typical used for the Altmark site) as given in Table 1. We used  $\rho^s = 2650 \text{ kgm}^{-3}$ ,  $c_p^s = 925 \text{ Jkg}^{-1}\text{K}^{-1}$ ,  $\kappa^s = 2.36 \text{ Wm}^{-1}\text{K}^{-1}$ ,  $n = 0.01$  and  $k = 9.8692 \times 10^{-15} \text{ m}^2$  for each non-injection layers.

Initially, pores of the solid skeleton are occupied by nitrogen and methane gases. Under the symmetric condition, a two-dimensional ( $x - z$ ) plane is extracted from the gas reservoir and injection well S13 is located at the left of this plane. The bottom of this plane is located at  $-3500\text{m}$  depth from the reservoir surface, and its height and length are 176m and 250m, respectively. For analysis of JTC and VHD effect, we alter the length of this plane by 1000m to visualize JTC and VHD effect for a longer time of injection. Geometrical details and conditions are given in Fig. 1. This plane was discretized with 44125 quad type elements. In the  $z$ -direction a constant step size is used, i.e.  $\Delta z = 0.5 \text{ m}$ . To capture the sharp gradient of the physical quantity close to the injection point, we used step size in the  $x$ -direction whereas ( $\Delta x$ ) varying from 0.001 m (at the injection point) to 10 m. For time stepping, we used a stable and efficient automatic time control algorithm based on elementary local error control theory described by Wang et al. (2011b); Söderlind (2002). Carbon dioxide

injection rate at the well S13 is equal to 142.86 tons per day at reservoir pressure of  $4.0 \times 10^6$  Pa and temperature of 125 °C. Assuming a density of  $94.896 \text{ kgm}^{-3}$ , which corresponds to a bottom-hole injection pressure of  $5.8 \times 10^6$  Pa at 102 °C, this gives  $0.017424 \text{ m}^3\text{s}^{-1}$  injection rate for numerical simulation of carbon dioxide injection. For verification of the numerical module with Eq. (4), we selected a simple example of an one-dimensional horizontal reservoir column to demonstrate the JTC effect. The comparison of steady state profile against the analytical solution (Singh et al. (2011)) for pressure and temperature (heat loss due to JTC) is presented in Fig. 2. In this example,  $\beta_T = 0.003 \text{ K}^{-1}$  is used for thermal expansion coefficient of gas. The initial temperature for injecting fluid and formation is equal to 125 °C.

#### 4.1 Joule-Thomson process

Understanding of the thermodynamical effect related to pressure change during compressible flow is essential for safe and optimal design of gas reservoir systems. As gas expands, average molecular distance grows, hence, potential energy increases due to growth of the intermolecular attractive forces. Total energy is conserved, therefore increased potential energy forces a decrease of kinetic energy, and thereby the gas cools down. Also, gas expansion reduces the frequency of molecular collision which causes a reduction in the average kinetic energy and fluid temperature decreases. For a thermodynamic system, when the temperature is below to the Joule-Thomson inversion temperature, a cooling effect dominates. Above this inversion temperature, collision frequency rises with the increase of molecular movement and therefore the JTC effect heats the gas. Hence, a fluid cools or heats upon expansion, depending on the value of its Joule-Thomson coefficient. Thermodynamically, the Joule-Thomson process conserves enthalpy. The Joule-Thomson coefficient is defined as the isenthalpic change in temperature of a fluid caused by a unitary pressure change, i.e.

$$\mu_{JT} = \left( \frac{\partial T}{\partial p} \right)_h \quad (15)$$

Fluid thermal expansivity  $\beta_T$  and Joule-Thomson coefficient  $\mu_{JT}$  can be thermodynamically related through the following expression:

$$\mu_{JT} = \frac{T\beta_T - 1}{\rho c_p} \quad (16)$$

Eq. (16) defines whether a fluid can be cooled down or warmed up upon expansion. When  $T\beta_T - 1$  is positive, the free expansion of the fluid leads to cooling. Consequently, for ideal gas  $\beta_T = 1/T$  gives  $\mu_{JT} = 0$ .

In this section we analyze the JTC effect by neglecting term  $n\mathbf{v} \cdot \nabla p$  from Eq. (4). Temperature contour corresponding to the JTC effect while injecting carbon dioxide in the gas reservoir is presented in Figs. 3a-d for different time steps. As injection begins, in the absence of thermal gradients, advection and conduction are not active. Hence, cooling occurs around the injection well at the start of the injection (see Fig. 3a) due to JTC. The extent to which pressure change can cool the reservoir layers is inversely proportion to the 'effective volumetric heat capacity' of the layer. Therefore, injection layers cool down more than non-injection layers and a plume with low temperature advances towards the observation well while exchanging heat with the reservoir through conduction.

To analyze the thermal interaction between injection and non-injection layers, in Fig. 4a we presented the temperature evolution at the observation points. These points are located in the layers B14a and NB14a along the well S13 with coordinates  $(0, -3436.6 \text{ m})$  and  $(0, -3431 \text{ m})$ , respectively (see Fig. 1). The curve corresponding to B14a and NB14a in Fig. 4a represents the time evolution of the temperature at the observation points located in layers B14a and NB14a, respectively. This figure shows that the rate of cooling in the non-injection layer NB14a is lower than in the injection layer B14a. For a very short duration (up to two days), Fig. 4a shows that JTC dominates, whereas for longer times, conduction raises the temperature near the injection well. However, for longer time, i.e. 30 days, the presented curves show that temperature values at both observation points are same. This reveals that there is heat exchange (through conduction) between the layers B14a and NB14a. Fig. 4b represents temperature profiles along the layer B14a for different time steps. The curve for 1 day shows a large temperature reduction in the vicinity of the injection well that is not affecting the undisturbed fluid temperature. Close to the injection well, temperature increases (due to conduction) while JTC cooling advances toward the observation point. The reason behind temperature rise is that the cooled area starts taking heat from the solid matrix.

#### 4.2 Viscous heat dissipation

In a viscous fluid flow, the viscosity of the fluid takes energy from the motion of the fluid (kinetic energy) and transforms it into internal energy of the fluid (viscous heat dissipation). The viscous heat dissipation process is partially irreversible and is high in regions with a large pressure gradient. So, in the case of carbon dioxide gas injection, fluid close to the inlet heats up.

In this section we omitted the terms,  $n\beta_T T \frac{\partial p}{\partial t}$  and  $\beta_T T n \mathbf{v} \cdot \nabla p$  from Eq. (4). In Figs. 5a-d we present the temperature contours due to VHD heating. Fig. 5a shows that at the beginning of injection, fluid flows in the injection layers with larger velocity than in non-injection layers according to their intrinsic permeability. Hence, VHD behaves differently in the different layers of the reservoir, i.e. more heating can be observed in highly permeable layers compared to low permeability layers. For longer injection times, the pressure field becomes uniform, consequently, whatever heat that was generated due to VHD is diffused among the reservoir layers at a rate dependent on the effective thermal diffusivity ( $\alpha_{\text{eff}} = n\alpha + (1-n)\alpha^s$ ) of the layer. The values of  $\alpha_{\text{eff}}$  for injection and non-injection layers are approximately the same. Therefore, plots for longer injection times, i.e. Figs. 5b-d, show that the temperature difference between injection and non-injection layers is decreasing.

In Fig. 6a we plotted viscous heating versus time at both observation points. Curves in this figure show sharp increments before 30 days of injection. After this time flow velocity weakens and whatever heat has generated due to VHD starts diffusing. Due to this diffusion, a small reduction in the temperature is observed after 30 days. Fig. 6b clearly shows that VHD increases the reservoir temperature. The distance from the injection point that VHD can heat the reservoir depends on the rate of gas injection and amount of gas injected. For example, at the considered injection rate, in one day VHD is able to heat the reservoir layer B14a only up to 200m from the injection well. For longer injection periods, i.e. 7 or 30 days, VHD is able to heat the whole layer.

These profiles also show that near the injection well (where flowing velocity is large), the heating extent is higher than in the rest of layer B14a.

JTC and VHD processes affect the reservoir temperature in mutually opposite ways. To determine which one is dominant in the scenario of carbon dioxide sequestration, we produced the temperature profile along the layer B14a using the full form of the Eq (4) and presented in Fig. 7. The temperature profiles at the 1<sup>st</sup> day and 7<sup>th</sup> day show that temperature is below the initial reservoir temperature value, i.e. 125 °C, whereas temperature profiles for the 30<sup>th</sup> day are also below the initial temperature except near the injection well. Hence, JTC dominates over VHD.

### 4.3 Warm-back behavior

Numerical simulation for warm-back analysis (without JTC and VHD) is divided into two parts to mimic the different operation regimes. In the first part we inject carbon dioxide for a duration of 10 days, i.e. the injection regime. In the second part, the temperature solution at the end of the injection regime is used as the initial temperature while setting a constant pressure over the whole computational domain, i.e. the shut-in regime. The purpose of the shut-in period is to suppress/eliminate the advective portion of heat transport. Hence, heat transport during the shut-in regime is only by conduction. By shutting the well for a period of 100 days, we record the transient temperature response during the warm-back. The different warm-back behavior is a function of the shut-in time, previous injection time, injection rate and temperature, as well as hydraulic and thermal properties of the reservoir rock and the injected carbon dioxide. Using these parameters, numerical simulation provides the opportunity to calculate the warm-back behavior of different layers depending on the injectivity of each layer. The injection regime is mostly controlled by the injection rate at given pressure and temperature conditions of the reservoir formation. We used an analytical solution by Köckritz (1979) to find the injecting fluid temperature. This analytical solution describes conductive heat transfer between formation and injected fluid.

Pressure and temperature distributions at the end of the injection regime are presented in Figs. 8a, b. Fig. 8a shows stronger pressure propagation in injection layers than non-injection layers. This figure also depicts negligible gravity effects on fluid flow, which negates possible inter-layer flow. As expected from the pressure propagation, Fig. 8b shows that during injection, heat transport in injection layers is mainly due to advection, whereas in non-injection layers conduction is the main phenomenon of heat transport. Heat propagation, however, is very weak in comparison to pressure because of the very high 'effective volumetric heat capacity'  $(\rho c_p)_{\text{eff}}$  of the reservoir layers.  $(\rho c_p)_{\text{eff}}$  depends primarily on the porosity value; accordingly, non-injection layers have larger 'effective volumetric heat capacity' than injection layers. To show the heat propagation in the reservoir layers, in Fig. 9a we have presented temperature profiles along the center line of the injection layer B14a and its neighboring non-injection layer, i.e. NB14a. We find that during injection the permeable layer B14a cooled with a greater radius than the impermeable layer NB14a (see temperature difference at  $x = 3\text{m}$  in Fig. 9a). Here it is important to see how reservoir layers behave with respect to conductive heat transport during the shut-in period. To this end, in Fig. 9b we have presented temperature profiles in B14a and NB14a at the 10<sup>th</sup> day of the shut-in regime. We find that warm-back is stronger in the non-injection layers than injection layers.

For the case of multi-componential fluid, temperature contours during the shut-in period of the 1<sup>st</sup> day; 10<sup>th</sup> day and 100<sup>th</sup> day are presented in Fig. 10. Plots for different times show that during shut-in, heat is flowing back to the injection well. However, non-injection layers warm-back at much faster rates than the non-permeable layers. Though, for longer periods of time Fig. 10c depicts that the temperature distribution is almost uniform. In the above case of a simplified reservoir we have used constant material parameters with an assumption that the formation fluid is pure carbon dioxide. In the case of multi-componential fluid flow (THC<sup>n</sup>) we used variability of material parameters (w.r.t pressure, temperature and mixture composition), and the formation fluid is a mixture of CH<sub>4</sub> and N<sub>2</sub> in composition of 25% and 75%. Fig. 11 illustrates shut-in temperature profiles along the injection well S13 during a shut-in period of the 1<sup>st</sup> day; 10<sup>th</sup> day and 100<sup>th</sup> day. This figure includes the shut-in temperature profiles from the FeFlow and OGS simulators for the case of a simplified reservoir. Shut-in temperature profiles from both simulators are in close agreement. This figure also presents the componential effect on the warm-back behavior. From the results it is clear that the multi-componential effect produces stronger warm-back in the injection layers while warm-back in the non-injection layers remains unchanged. The figure clearly reveals that the extent of warm-back towards the well by conduction through non-injection layers dominates over the injection layer. Time series of temperature (during the shut-in period) for the cases of simplified and multi-componential are presented in Fig. 12. In addition, the figure shows that at the beginning the strength of warm-back is very high but weakens with time and ultimately the temperature at observation points reaches the reservoir temperature. Occasionally information about the thermal gradient in a particular layer is important. For that we have presented the temperature profile along layer B14a at different time steps during the shut-in period in Fig. 13. The profile for a one day shut-in time illustrates that the thermal gradient along layer B14a is very high, but other temperature profiles, i.e. for the 10<sup>th</sup> and 100<sup>th</sup> day show that the layer achieves thermal equilibrium.

## 5 Conclusions and outlook

In this work, reservoir temperature was altered significantly due to carbon dioxide injection. Particularly, conductive warm-back during the shut-in regime gradually increased the temperature near the wellbore region. Change in the reservoir temperature was observed due to reservoir repressurization (decreased due to JTC and increased due to VHD).

### 5.1 Achievements

In the present work warm-back behavior, JTC, and VHD effects have been analyzed thus far. The following progress was achieved.

1. JTC and VHD effects altered static formation temperature near the injection well. JTC cools where VHD heats the formation. Temperature change due to these effects was different in different layers. A larger temperature change was observed in injection layers compare to non-injection layers, as pressure drops in the non-injection layers was mild. The magnitude at which pressure change could change

the temperature was directly governed by the 'effective volumetric heat capacity' of the layer.

2. Because of the lower volumetric heat capacity of the injection layers compare to non-injection layers, JTC cooled injection layers faster than non-injection layers. Heat transfer owing to pressure drop is very fast, therefore, JCT and VHD processes were assumed as isenthalpic processes. Heat lost (or gained) in the formation fluid by JCT (or VHD) was diffused in the solid matrix with a diffusion rate which was dependent upon the respective layers' effective thermal diffusivity,  $\alpha_{\text{eff}} = n\alpha + (1 - n)\alpha^s$ . Hence, there must be exchange of heat (by conduction) between two adjacent layers.
3. In general the porosity was a crucial driver for temperature propagation, i.e. the larger the porosity (and permeability) the more cold carbon dioxide went into the layer. Hence, during the injection regime, injection layers cooled with a greater radius. In the shut-in regime, conductive warm-back was found stronger in non-injection layers (because of larger effective conductivity value) compare to injection layers. Multi-componential effects produced little stronger warm-back.
4. Warm-back behavior showed a significant change in reservoir temperature during and after carbon dioxide gas injection. Temperature change in the injection regime was mainly because of the relatively lower temperature of the injected carbon dioxide. Results of warm-back behavior were proposing to account thermal effect for injection monitoring.

## 5.2 Outlook

In addition to the achievements above, the presented model has some limitations concerning parameterizations and its current applicability.

1. The model accounts only for conductive heat transport during the shut-in regime while ignoring the advective part of heat transport by setting a constant pressure over the whole domain. Warm-back behavior of the gas reservoir with advective heat transport during the shut-in regime could be important.
2. Results in sections 4.1 and 4.2 were based on a thermal equilibrium assumption between injected and formation fluids at the start of injection. This assumption was just for visualization of the JTC and VHD effects in the gas reservoir. In reality, injecting fluid is cooler than the formation. In this scenario advective and conductive heat transport dominate over JTC and VHD.
3. The model used a constant value for the thermal expansivity  $\beta_T$  for the considered gas mixture. Inclusion of its variability w.r.t. pressure, temperature and mixture composition would give a more accurate JTC effect. The model needs to be extended in this manner, which is the focus of future work.

**Acknowledgements** :The authors acknowledge the funding by the German Federal Ministry of Education and Research (BMBF) in the framework of the CLEAN joint project, which is part of the geoscientific R&D program GEOTECHNOLOGIEN (results are presented in the GEOTECHNOLOGIEN Scientific Report under the publication number GEOTECH-1951). We would like to thank Guido Blöcher for his support with the FeFlow simulation and Alissa Hafele for English correction.

## References

- Ahmed A, Lee WJ (1995) Development of a new theoretical model for three-layered reservoirs with unequal initial pressures. SPE **29463-MS**.
- Andre L., Azaroual M, M Menjoz (2010) Numerical Simulations of the Thermal Impact of Supercritical CO<sub>2</sub> Injection on Chemical Reactivity in a Carbonate Saline Reservoir. *Transp Porous Media* **82**: 247 - 274.
- Böttcher N, Singh AK, Kolditz O, Liedl R (2011) Non-isothermal, compressible gas flow for the simulation of an enhanced gas recovery application. *J Comp App Math* DOI:10.1016/j.cam.2011.11.013.
- Becker V, Myrntinen A, Zimmer M, Barth JAC (2012) Stable isotope applications during carbon capture and storage (CCS) and enhanced recoveries of hydrocarbons. *Environ Earth Sci* (submitted).
- Cui C, Zhao X (2010) Method for calculating production indices of multilayer water drives reservoirs. *J Pet Sci Eng* **75**:66-70.
- Curtis MR, Witterholt EJ (1973) Use of the temperature log for determining flow rates in production wells. SPE **4637-MS**.
- Ehlig-Economides CA, Joseph JA (1987) A new test for determination of individual layer properties in a multi-layered reservoir. *SPE Formation Evaluation* **2**:261-283.
- Esposito RA, Pashin JC, Hills DJ, Walsh PM (2010) Geologic assessment and injection design for a pilot CO<sub>2</sub>-enhanced oil recovery and sequestration demonstration in a heterogeneous oil reservoir: Citronelle Field, Alabama, USA. *Environ Earth Sci* **60**:431 - 444.
- Garg SK, Pritchett JW (1977) On pressure-work, viscous dissipation and the energy balance relation for geothermal reservoirs. *Adv Water Res* **1**:41-47.
- Gray WG, Miller CT (2004) Examination of Darcy's law for flow in porous media with variable porosity. *Environ Sci Technol* **38**:5895-5901.
- GDF SUEZ (2009) CLEAN DMS data mangement system. GFZ German Research Center for Geosciences.
- Görke U-J, Park C-H, Wang W, Singh AK, Kolditz O (2011) Numerical simulation of multi-phase hydro-mechanical processes induced by CO<sub>2</sub> injection into deep saline aquifers. *Oil & Gas Science and Technology* **66**:105-118.
- Helmig R (1997) *Multi-Phase Flow and Transport Processes in the Subsurface: a Contribution to the Modeling of Hydro-Systems*. Springer-Verlag Berlin Heidelberg.
- Henniges J, Baumann G, Brandt W, Cunow C, Poser M, Schrötter J, Huenges E, (2011) A novel hybrid wireline logging system for downhole monitoring of fluid injection and production in deep reservoirs. In: proceeding of 73<sup>rd</sup> EAGE Conference & Exhibition, Vienna, Austria.
- Henniges J, Baumann G (2012) Well logging for injection and saturation profiling during CO<sub>2</sub> injection in depleted gas fields. *Environ Earth Sci* (submitted).
- Hurter S, Garnett A, Bielinski A, Kopp A (2007) Thermal signature of free-phase carbon dioxide in porous rocks: detectability of carbon dioxide by temperature logging. SPE **109007-MS**.
- Kolditz O, Diersch HJ (1993) Quasi steady-state strategy for numerical simulation of geothermal circulation processes in hot dry rock fracture. *Int J Non Linear Mech* **28**: 467-481.
- Kolditz O, Bauer S, Beyer C, Böttcher N, Görke U-J, Kalbacher T, Park CH, Singh AK, Taron J, Wang W, Watanabe N (2012) A systematic benchmarking method for geologic CO<sub>2</sub> injection and storage. *Environ Earth Sci* DOI: 10.1007/s12665-012-1656-5.
- Köckritz V. (1979) *Wärmeübertragungs- und Strömungsvorgänge bei der Förderung und Speicherung von Gasförmigen Medien - ein Beitrag zur Mathematischen Modellierung des Druck- und Temperaturverhaltens in Fördersonden und Speicherkavernen*. Dissertation, Freiberg.
- Kuchuk FJ, Goode PA, Wilkinson DJ, Thambynayagam RKM (1991) Pressure-transient behavior of horizontal wells with and without gas cap or aquifer. *SPE Formation Evaluation* **6**:86-94.
- Kühn M, Förster A, Grossmann J, Meyer R, Reinicke K, Schäfer D, Wendel H (2011) CLEAN: Preparing for a CO<sub>2</sub> based enhanced gas recovery in a depleted gas field in Germany. *Energy Procedia* **4**:5520-5526.
- Kühn M, Tesmer M, Pilz P, Meyer R, Reinicke K, Förster A, Kolditz O, Schäfer D (2012) Overview of the joint research project CLEAN: CO<sub>2</sub> Large-Scale Enhanced Gas Recovery in the Altmark natural gas field (Germany). *Environ Earth Sci* (submitted).

- Lefkovits HC, Hazebroek P, Allen EE, Matthews CS (1961) A study of the behavior of bounded reservoirs composed of stratified layers. *SPE Journal* **1**:43-58.
- Mathias SA, Gluyas JG, Oldenburg CM, Tsang C (2010) Analytical solution for Joule-Thomson cooling during carbon dioxide geo-sequestration in depleted oil and gas reservoirs. *Int J Greenhouse Gas Control* **4**:806-810.
- Millington RJ, Quirk JP (1961) Permeability of porous solids. *Trans Faraday Soc* **57**:1200-1207.
- Oldenburg CM (2007) Joule-Thomson cooling due to CO<sub>2</sub> injection into natural gas reservoirs. *Energy Convers Manage* **48**:1808-1815.
- Oldenburg CM, S.H Stevens SH, S.M Benson SM (2004) Economic feasibility of carbon sequestration with enhanced gas recovery (CSEGR). *Energy* **29**:1413-1422.
- Ouyang LB, Belanger DL (2006) Flow profiling by distributed temperature sensor (DTS) system-expectation and reality. *SPE Production & Operations* **21**:269-281.
- Park C-H, Böttcher N, Wang W, Kolditz O (2011) Are upwind techniques in multi-phase flow models necessary? *J Comp Physics* **30**:8304-8312.
- Pruess K (2008) On carbon dioxide fluid flow and heat transfer behavior in the subsurface, following leakage from a geologic storage reservoir. *Environ Geol* **54**:1677-1686.
- Ramazanov A Sh, Nagimov VM (2007) Analytical model for the calculation of temperature distribution in the oil reservoir during unsteady fluid inflow. *Oil Gas Bus J*.
- Ramey Jr. H (1962) Wellbore heat transmission. *J Pet Tec* **96**:427-35.
- Söderlind G (2002) Automatic control and adaptive time-stepping. *Numerical Algorithms* **31**:281-310.
- Rink K, Kalbacher T, Kolditz O (2011) Visual data exploration for hydrological analysis. *Environ Earth Sci* **65**:1395-1403.
- Singh AK, Görke U-J, Kolditz O (2011) Numerical simulation of non-isothermal compositional gas flow: Application to CO<sub>2</sub> injection into gas reservoirs. *Energy* **36**:3446-3458.
- Singh AK, Pilz P, Zimmer M, T. Kalbacher Görke U-J, Kolditz O (2012) Numerical simulation and geophysical monitoring of tracer transport in the Altmark gas field. *Environ Earth Sci* (submitted).
- Sui W, Zhu D, Hill AD, Ehlig-Economides CA (2008) Determining multilayer formation properties from transient temperature and pressure measurements. In: proceeding of SPE Annual Technical Conference and Exhibition, 21-24 September 2008, Denver, Colorado, USA.
- Tenzen H, Park C-H, Kolditz O, McDermott CI (2010) Comparison of the exploration and evaluation of enhanced HDR geothermal sites at Soultz-sous-Forts and Urach Spa. *Environ Earth Sci* **61**: 853-880.
- Vargaftik, NB (1975) Tables on the Thermo Physical Properties of Liquids and Gases. 2<sup>nd</sup> edn. New York, Hemisphere Publication Corporation.
- Wang W, Rutqvist J, Görke U-J, Birkholzer JT, Kolditz O (2011) Non-isothermal flow in low permeable porous media: a comparison of Richards' and two-phase flow approaches. *Environ Earth Sci* **62**:1197-1207.
- Wang W, Schnicke T, Kolditz O (2011) Parallel finite element method and time stepping control for non-isothermal poro-elastic problems. *Comput Mate Continua* **21**:217-235.
- Witterholt E, Tixier M (1972) Temperature logging in injection wells. In: proceeding of Fall Meeting of the Society of Petroleum Engineers of AIME, 8-11 October 1972, San Antonio, Texas.
- Wooding RA (2006) Steady state free thermal convection of liquid in a saturated permeable medium. *J Fluid Mech* **2**:273-285.
- Yang YM, Small MJ, Junker B, Bromhal GS, Strazisar B, Wells A (2011) Bayesian hierarchical models for soil CO<sub>2</sub> flux and leak detection at geologic sequestration sites. *Environ Earth Sci* **64**:787 - 798.

---

**List of figures caption**

- Fig.1 Model setup for carbon dioxide injection at multi-layered depleted gas reservoir.
- Fig.2 Comparisons of steady state profiles against analytical solution for pressure and temperature (due to JTC) in a 100 m long one-dimensional horizontal reservoir column.
- Fig.3 Temperature ( $^{\circ}\text{C}$ ) distribution due Joule-Thomson cooling effect around the injection well S13 for (a) day; (b) week (c) month and (d) 100 days of injection time.
- Fig.4 (a) Joule-Thomson cooling versus time at observation points located in Layers B14a and NB14a; (b) Joule-Thomson cooling profiles along the most permeable layer B14a.
- Fig.5 Temperature ( $^{\circ}\text{C}$ ) distribution due viscous heat dissipation around the injection well S13 for (a) day; (b) week (c) month and (d) 100 days of injection time.
- Fig.6 (a) Viscous heating versus time at observation points located in Layers B14a and NB14a; (b) viscous heating profiles along the most permeable layer B14a.
- Fig.7 Temperature profiles along the most permeable layer B14a, for combined effect of Joule-Thomson cooling and viscous heat dissipation.
- Fig.8 Distribution of (a) pressure (Pa) and (b) temperature ( $^{\circ}\text{C}$ ) around the injection well S13 at the end of injection for the warm-back analysis.
- Fig.9 Temperature profiles along most and least permeable layers, i.e. B14a and NB14a (a) at end of injection period (b) at 10<sup>th</sup> day of shut-in period.
- Fig.10 Temperature ( $^{\circ}\text{C}$ ) distribution due to warm-back effect around the injection well S13 for (a) 1<sup>st</sup> day; (b) 10<sup>th</sup> day and (c) 100<sup>th</sup> day of shut-in regime.
- Fig.11 Comparison of shut-in temperature profiles from the FEM solution of OGS and FeFlow simulators along with multi-compartmental effect. (a) 1<sup>st</sup> day; (b) 10<sup>th</sup> days and (c) 100<sup>th</sup> day of shut-in regime.
- Fig.12 Time series of warm-back at observation points located in the layer B14a for simplified reservoir and multi-compartmental effect.
- Fig.13 Temperature profile along the most permeable layer B14a, at three different shut-in time.

## Appendix

Elements of mass, advection, Laplace matrices and right hand side vectors of the Eqs. (9)-(11) are as follow:

$$\begin{aligned}
\mathbf{C}_{pp} &= \int_{\Omega} \mathbf{N}^T \left[ n \frac{1}{\rho} \frac{\partial \rho}{\partial p} \right] \mathbf{N} d\Omega \\
\mathbf{C}_{pT} &= \int_{\Omega} \mathbf{N}^T \left[ n \frac{1}{\rho} \frac{\partial \rho}{\partial T} \right] \mathbf{N} d\Omega \\
\mathbf{K}_{pp} &= - \int_{\Omega} (\nabla \mathbf{N})^T \left[ \frac{k}{\mu} \right] \nabla \mathbf{N} d\Omega \\
\mathbf{K}_{pT} &= - \int_{\Omega} (\nabla \mathbf{N})^T [0] \nabla \mathbf{N} d\Omega \\
\mathbf{A}_{pp} &= \int_{\Omega} \mathbf{N}^T \left[ n \mathbf{v} \frac{1}{\rho} \frac{\partial \rho}{\partial p} \right] \nabla \mathbf{N} d\Omega \\
\mathbf{A}_{pT} &= \int_{\Omega} \mathbf{N}^T \left[ n \mathbf{v} \frac{1}{\rho} \frac{\partial \rho}{\partial T} \right] \nabla \mathbf{N} d\Omega \\
\mathbf{f}_p &= - \int_{\Omega} (\nabla \mathbf{N})^T \left[ \frac{k}{\mu} \rho \mathbf{g} \right] d\Omega - \int_{\partial \Omega} \mathbf{N} [Q_p] d\partial \Omega \\
\mathbf{C}_{Tp} &= \int_{\Omega} \mathbf{N}^T [-nT\beta_T] \mathbf{N} d\Omega \\
\mathbf{C}_{TT} &= \int_{\Omega} \mathbf{N}^T [(\rho c_p)_{\text{eff}}] \mathbf{N} d\Omega \\
\mathbf{K}_{Tp} &= - \int_{\Omega} (\nabla \mathbf{N})^T [0] \nabla \mathbf{N} d\Omega \\
\mathbf{K}_{TT} &= - \int_{\Omega} (\nabla \mathbf{N})^T [\kappa_{\text{eff}}] \nabla \mathbf{N} d\Omega \\
\mathbf{A}_{Tp} &= \int_{\Omega} \mathbf{N}^T [n \mathbf{v} (1 - T\beta_T)] \nabla \mathbf{N} d\Omega \\
\mathbf{A}_{TT} &= \int_{\Omega} \mathbf{N}^T [n \mathbf{v} \rho c_p] \nabla \mathbf{N} d\Omega \\
\mathbf{f}_T &= - \int_{\Omega} \mathbf{N} [Q_T] d\partial \Omega \\
\mathbf{C}_{xk} &= \int_{\Omega} \mathbf{N}^T [n\rho] \mathbf{N} d\Omega \\
\mathbf{K}_{xk} &= - \int_{\Omega} (\nabla \mathbf{N})^T [n\rho D] \nabla \mathbf{N} d\Omega \\
\mathbf{A}_{xk} &= \int_{\Omega} \mathbf{N}^T [n \mathbf{v} \rho] \nabla \mathbf{N} d\Omega \\
\mathbf{f}_{xk} &= - \int_{\Omega} \mathbf{N} [Q - x_k \rho Q_\rho] d\partial \Omega
\end{aligned}$$

**Table 1** Medium properties of injection layers.

---

Layers	$\Delta h(\text{m})$	$n(-)$	$k(\text{m}^2)$
17B	1	0.123	$9.8692 \times 10^{-15}$
16B	1.5	0.105	$9.8692 \times 10^{-15}$
A	3.5	0.110	$9.8692 \times 10^{-15}$
B14a	3	0.160	$9.8692 \times 10^{-14}$
B14b	5.5	0.155	$5.9215 \times 10^{-14}$
B13	9	0.165	$5.9215 \times 10^{-14}$
C12	1	0.155	$5.9215 \times 10^{-14}$

---

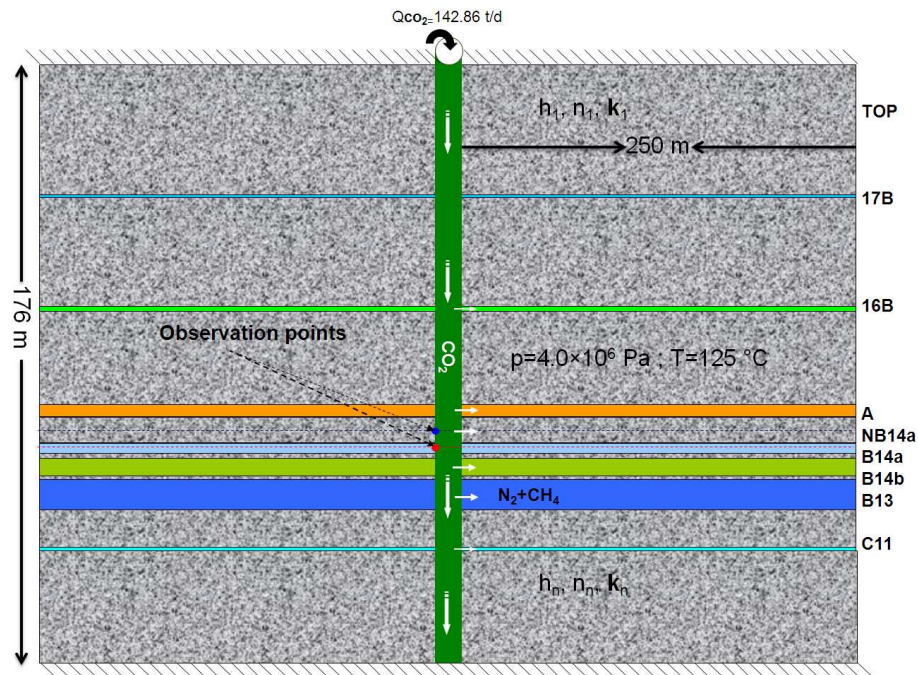


Fig. 1 Model setup for carbon dioxide injection at multi-layered depleted gas reservoir.

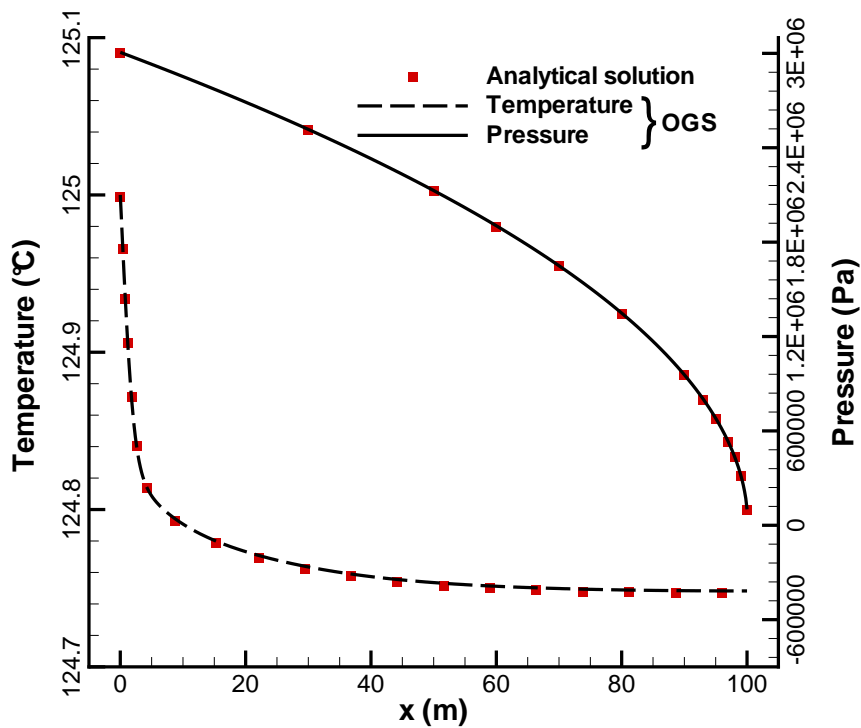


Fig. 2 Comparisons of steady state profiles against analytical solution for pressure and temperature (due to JTC) in a 100 m long one-dimensional horizontal reservoir column.

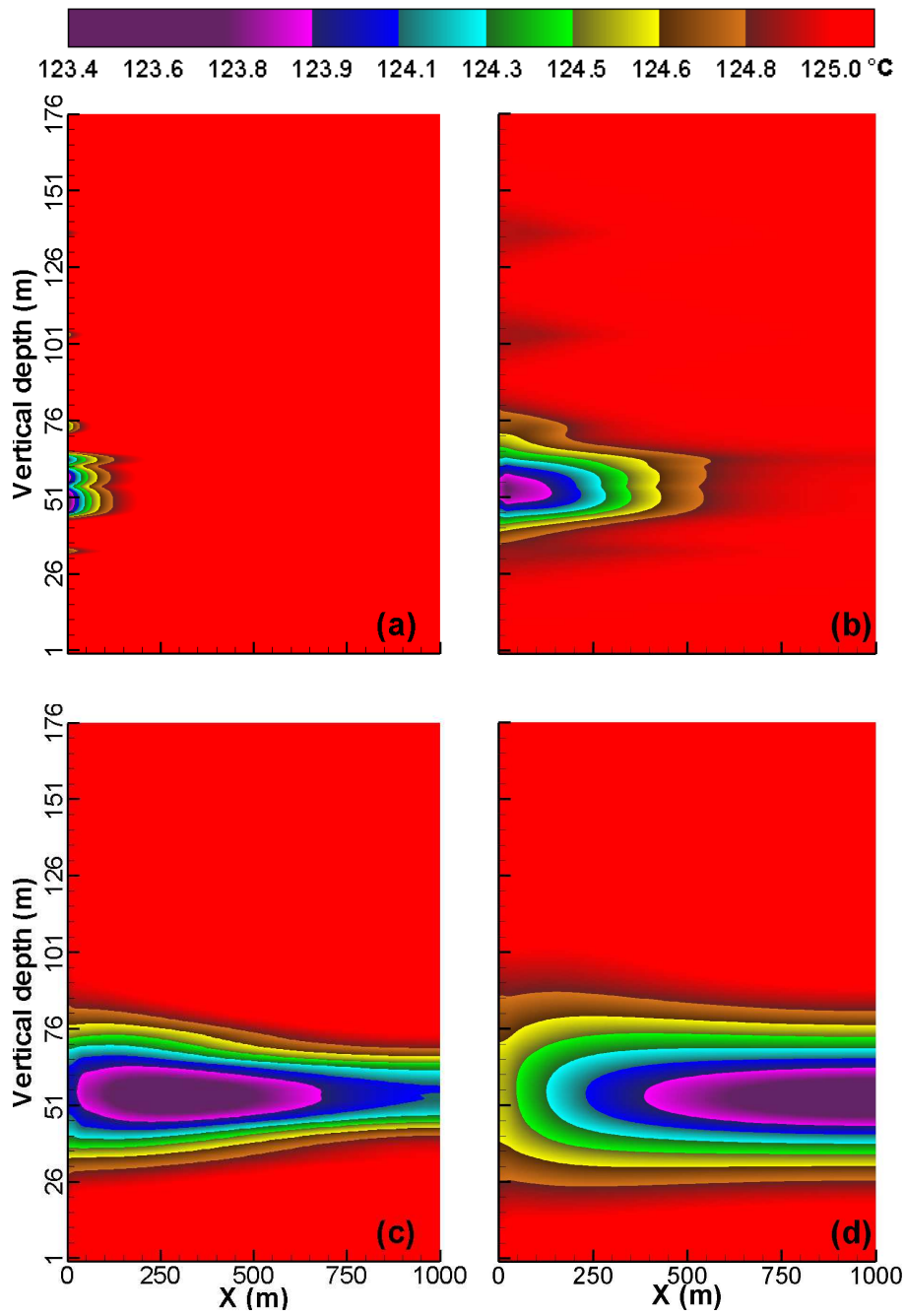


Fig. 3 Temperature ( $^{\circ}\text{C}$ ) distribution due to Joule-Thomson cooling effect around the injection well S13 for (a) day; (b) week (c) month and (d) 100 days of injection time.

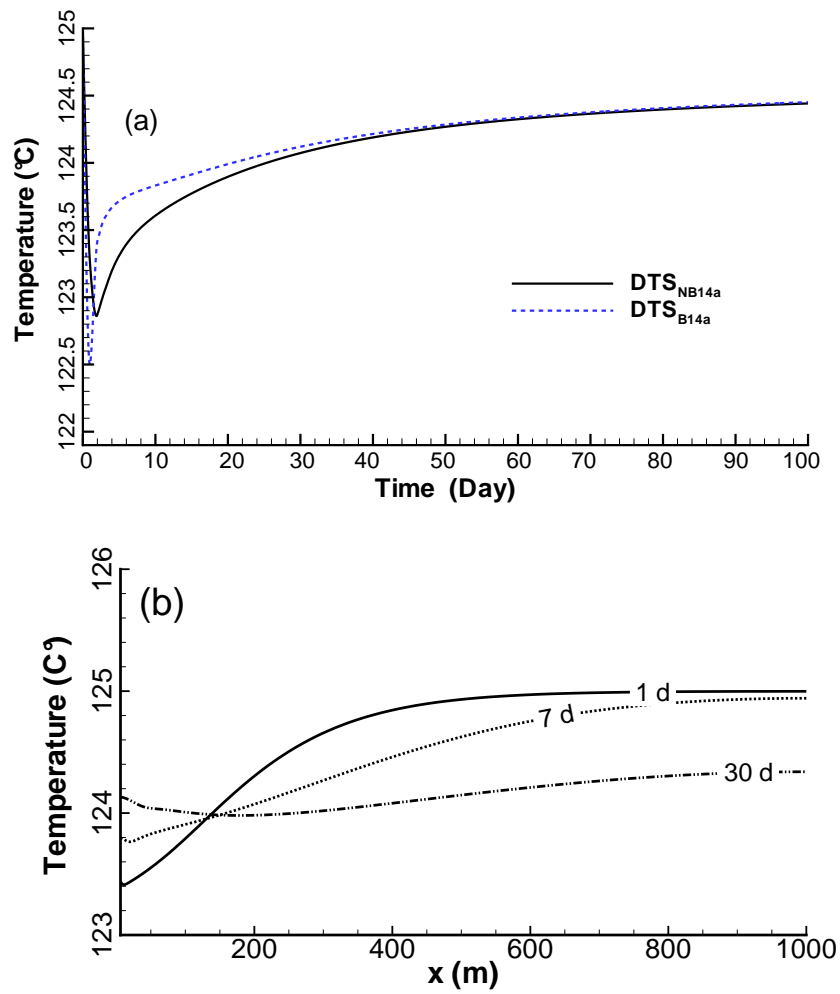


Fig. 4 (a) Joule-Thomson cooling versus time at observation points located in Layers B14a and NB14a; (b) Joule-Thomson cooling profiles along the most permeable layer B14a.

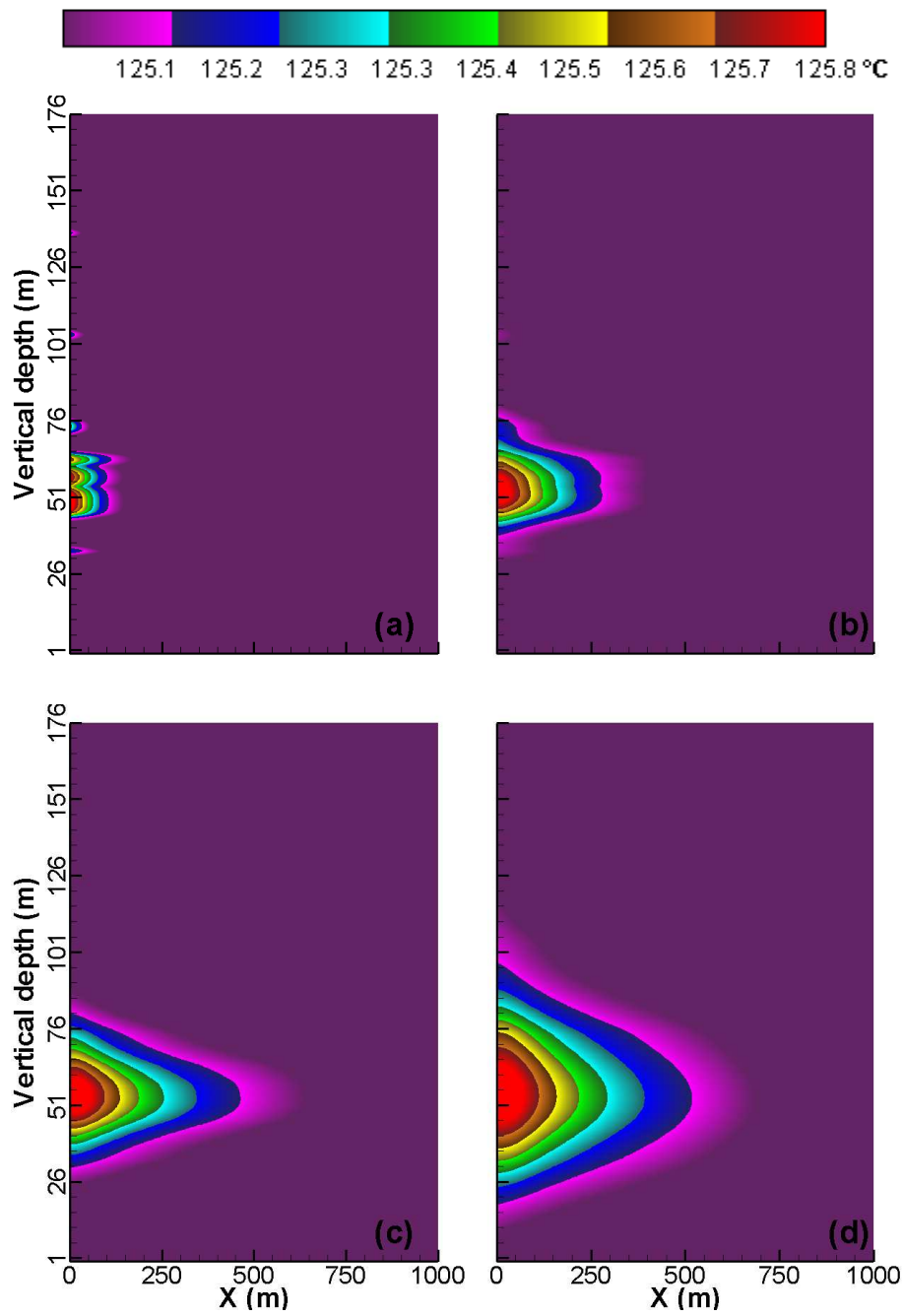
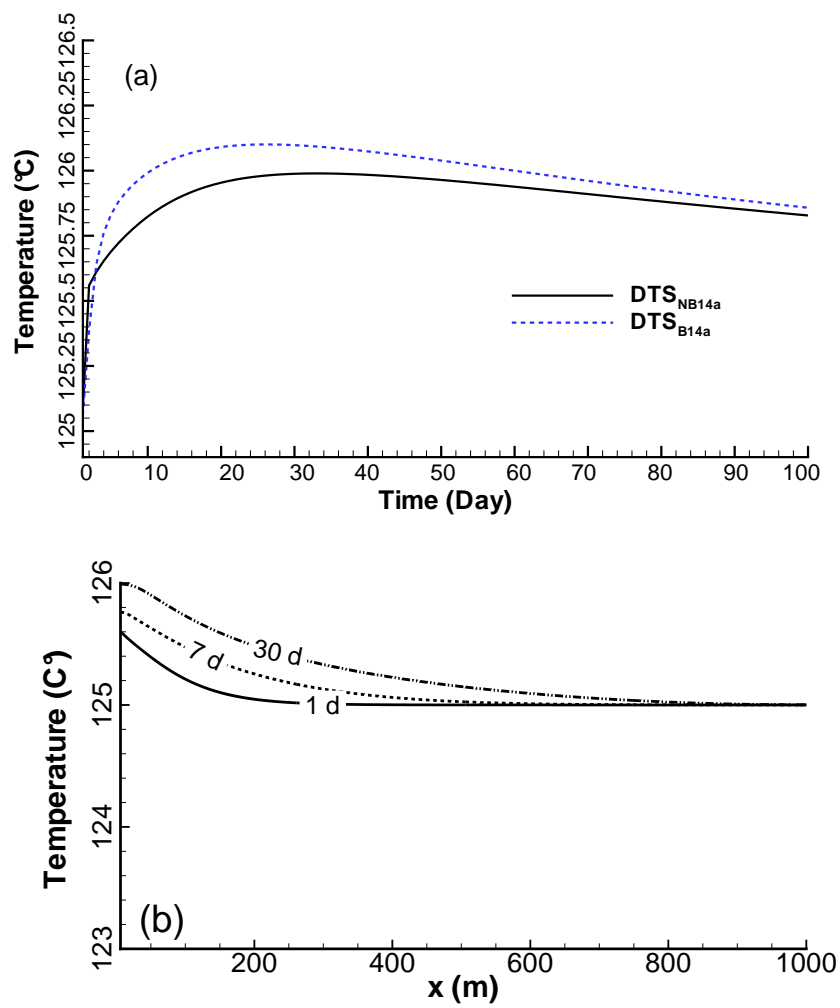


Fig. 5 Temperature ( $^{\circ}\text{C}$ ) distribution due to viscous heat dissipation around the injection well S13 for (a) day; (b) week (c) month and (d) 100 days of injection time.



**Fig. 6** (a) Viscous heating versus time at observation points  $DTS_{B14a}$  and  $DTS_{NB14a}$  located in layers B14a and NB14a, respectively; (b) viscous heating profiles along the most permeable layer B14a.

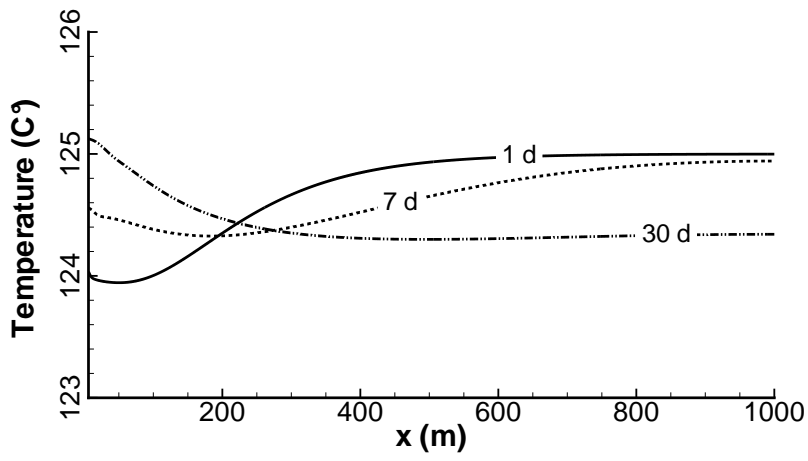


Fig. 7 Temperature profiles along the most permeable layer B14a, for combined effect of Joule-Thomson cooling and viscous heat dissipation.

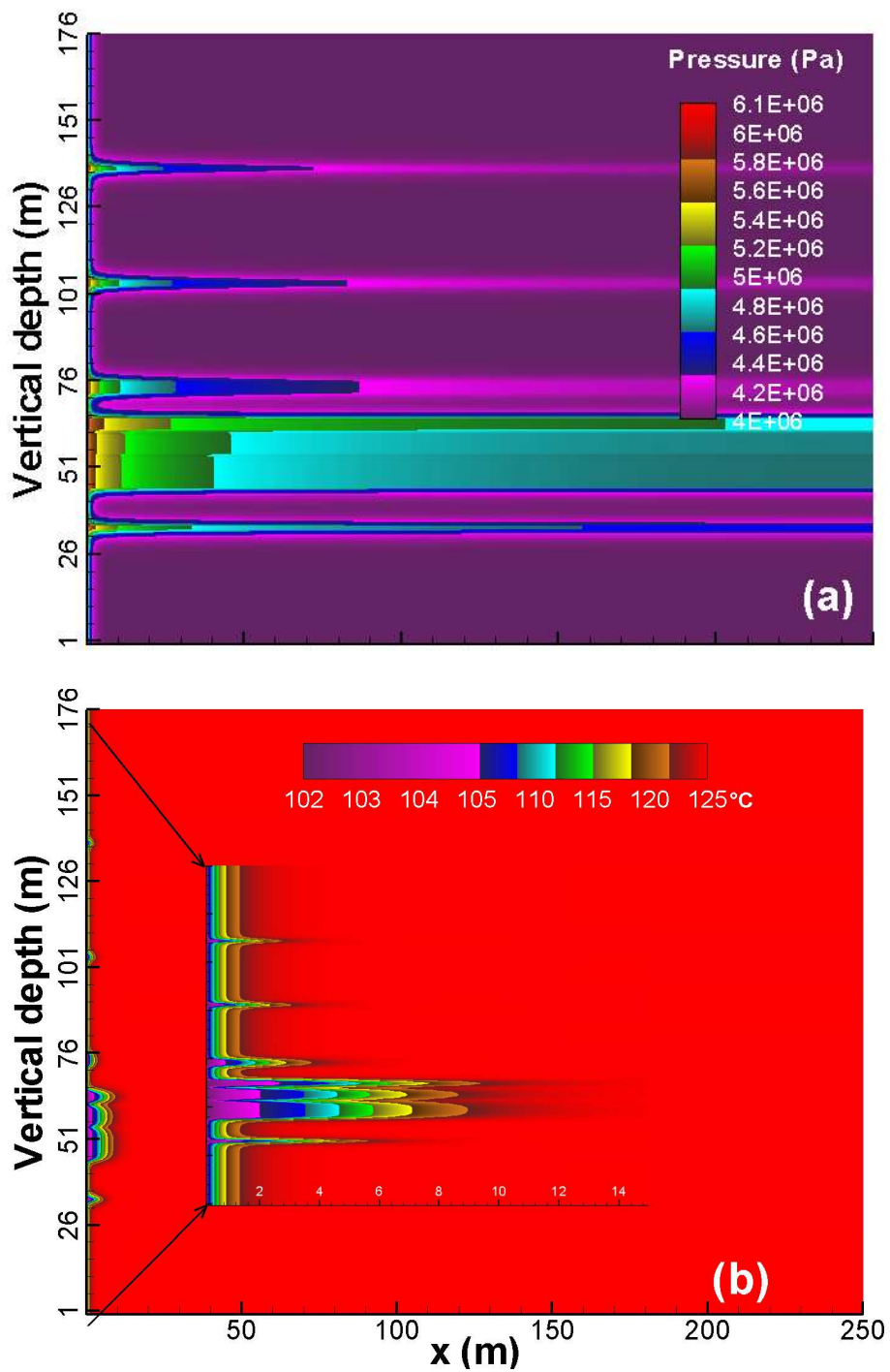
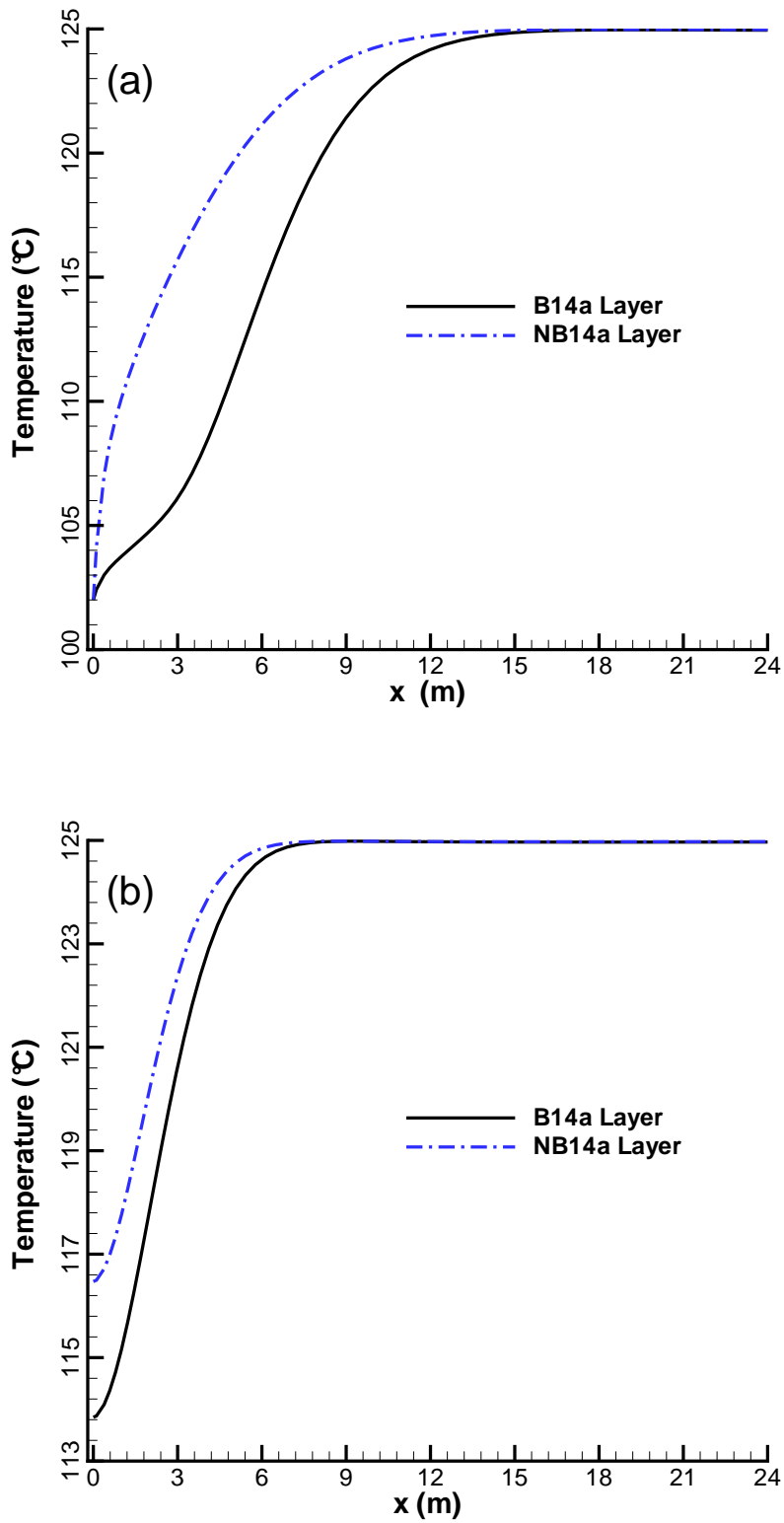


Fig. 8 Distribution of (a) pressure (Pa) and (b) temperature (°C) around the injection well S13 at the end of injection for the warm-back analysis.



**Fig. 9** Temperature profiles along most and least permeable layers, i.e. B14a and NB14a (a) at end of injection period (b) at 10<sup>th</sup> day of shut-in period.